

Strain-driven topological quantum phase transition in the family of halide perovskites

Ankita Phutela,^{*} Sajjan Shoeran, and Saswata Bhattacharya^{*}

Department of Physics, Indian Institute of Technology Delhi, New Delhi, India

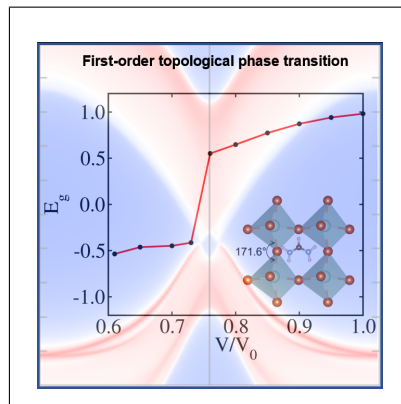
E-mail: Ankita@physics.iitd.ac.in[AP]; saswata@physics.iitd.ac.in[SB]

Phone: +91-11-2659 1359

Abstract

The centrosymmetric halide perovskites undergo a continuous phase transition from a normal insulator to a topological insulator at the critical value of strain. Contrarily, in noncentrosymmetric halide perovskites, this phase transition is discontinuous. The noncentrosymmetry does not stabilize the gapless state, causing a discontinuity in the bandgap. We have employed the density functional theory and Slater-Koster formalism-based tight-binding Hamiltonian studies to understand the evolution of band topology under the compressive strain in the halide perovskites. Our study shows that both cubic and pseudocubic FAPbI_3 undergo a Pb s - p band inversion at $\gamma (V/V_0) = 0.76$ and 0.73 , respectively. The cubic perovskite shows the surface state at \bar{M} , whereas, the pseudocubic structure shows two conducting states in the neighbourhood of \bar{M} , unlike the conventional topological insulator. The Pb-Pb second nearest neighbor interactions determine this topological phase transition. Alongside, we have modeled mixed cation halide perovskites $\text{Cs}_x\text{MA}_{1-x}\text{PbI}_3$ ($x = 0.25, 0.5$ and 0.75) to study their topological properties. $\text{Cs}_{0.5}\text{MA}_{0.5}\text{PbI}_3$ shows non-trivial topology at $\gamma = 0.74$. In addition, we have checked the structural stability of different strained configurations using *ab initio* molecular dynamics at operational temperature. Their structural stability under compression strengthens the experimental relevance.

Graphical TOC Entry



Keywords

Density functional theory, Spin-orbit coupling, Surface states, Strain, Topological insulator, Tight-binding model

Introduction

Topological phases of matter such as topological insulators¹, Dirac semimetals^{2,3}, Weyl semimetals^{4,5}, topological metals⁶, and topological crystalline insulators⁷ have occupied ample space in the research areas in the last two decades. Among these phases, topological insulators are one of the most promising materials for application in spintronics due to their conducting surface states within the bulk band gap⁸⁻¹⁰. Numerous materials like Bi-based selenides and tellurides^{11,12}, skutterudites¹³, Heusler compounds^{14,15}, and Bi-based oxide perovskites (ABiO₃)¹⁶⁻¹⁸ have been extensively explored for non-trivial topology. More recently, halide perovskites have also attracted attention for research in the area of band topology¹⁹. These are the compounds with the formula ABX₃, where A is an inorganic or organic cation, B is a heavy element, and X is a halogen. These materials are well known for their high performance in the field of optoelectronics, photovoltaics, photocatalysts, and thermoelectrics²⁰⁻²³. Their endeavors can be attributed to the compositional and structural diversity that enables a wide array of functional properties. They possess a suitable orbital symmetry and are structurally flexible to external stimuli such as pressure, temperature, and chemical doping, which make them useful in the field of topology^{18,24}. Furthermore, the molecular orbital picture of topologically non-trivial cubic ABiO₃, matches that of cubic halide perovskites (CsSnX₃)²⁵. However, unlike oxide perovskites, the *s-p* inversion on inclusion of spin-orbit coupling (SOC) is not shown by the halide perovskites. Therefore, the family of halide perovskites is not known to show topologically non-trivial phases at ambient conditions. Nevertheless, if we tune certain aforementioned external parameters, a topological phase can be realized in halide perovskites²⁶. It is consistent with the recent theoretical calculations that compressive strain can drive these materials into the topological insulator region²⁵. At a critical value of strain, a normal insulator to topological insulator (NI-TI) phase transition takes place. In materials preserving inversion symmetry, a continuous topological phase transition (TPT) take place²⁷. However, another type of phase transition, which is discontinuous in nature, has been observed in MAPbI₃ via application of pressure. It has been shown that in pseudocubic perovskites like MAPbI₃, the inversion symmetry breaking has a profound effect on the nature of phase transition¹⁹. The discontinuous phase

transition has also been observed in $\text{Pb}_{1-x}\text{Sn}_x\text{Se}$ and $\text{TlBiS}_{1-x}\text{Se}_x$ ^{28–31}. This is of key importance for device applications based on tuning the topological properties of the system by external means. Therefore, the realization of non-trivial phases under the effect of strain in pseudocubic perovskite will bring several families of compounds, beyond the intermetallic alloys, into the domain of research on band topology. This could be important in providing various heterostructure interfaces with multifunctional properties.

Motivated by this idea, we have looked for the NI-TI phase transition in FAPbI_3 (FA = formamidinium) under the effect of compressive strain. It has been found that the nature of TPT is continuous for cubic FAPbI_3 . But, when the centrosymmetry is broken in FAPbI_3 , an inverted band gap opens without closing to zero. The absence of inversion symmetry brings a first-order quantum phase transition on application of strain. We have applied volumetric strain to trigger this non-trivial topology, by inducing a band inversion in the bulk band structure. After that, the surface band structure is obtained to see the origin of surface states with increasing strain. To explore the underlying quantum mechanical process, which occurs due to structural deformation caused by the application of strain, Slater-Koster tight-binding (SK-TB) model have been employed. We have also designed the thermodynamically stable mixed cation halide perovskites with the formula $\text{Cs}_x\text{MA}_{1-x}\text{PbI}_3$ ($x = 0.25, 0.5, \text{ and } 0.75$). The bulk and surface band structures are plotted at different values of strain to observe the TPT. Afterward, the structural stability of all the unstrained and strained configurations at an operational temperature of 300K has been confirmed to signify their practical usage.

FAPbI_3 exists in cubic phase with $Pm\bar{3}m$ space group at 298 K with planar $[\text{H}_2\text{N-CH-NH}_2]^+$ cation surrounded by $[\text{PbI}_3]^-$ octahedra as shown in Figure 1(a). The lattice constant is taken as 6.32 \AA , which is in close agreement with the previous report³². The structural relaxation of FAPbI_3 carried out using DFT methods leads to a distortion in the octahedral cage, causing an asymmetry in the structure³³. The crystal structure becomes pseudocubic with Pb-I-Pb angle 171.6° as shown in Figure 1(b), which is similar to that of MAPbI_3 ¹⁹. The bulk Brillouin zone (BZ) showing the high symmetry k -points and the projected surface BZ is shown in Figure 1(c). The conduction bands

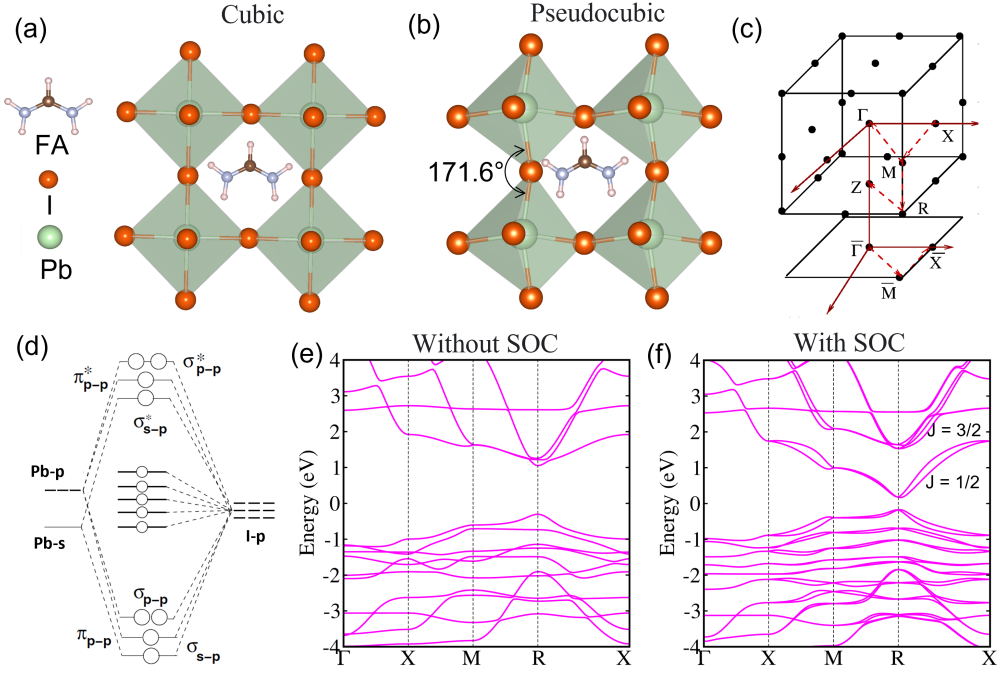


Figure 1: Crystal structure of (a) cubic and (b) pseudocubic FAPbI_3 . (c) 3D BZ along with the projected 2D BZ. (d) The molecular orbital picture for FAPbI_3 . Bulk band structure of FAPbI_3 in the (e) absence of SOC and (f) presence of SOC.

near the Fermi surface are mainly contributed by the Pb-6p orbitals, whereas the valence bands are mainly contributed by Pb-6s and I-5p orbitals³⁴. The energy states of other elements in FA are mainly distributed in the deep energy levels, and are not involved in bonding. The Pb- $\{s,p\}$ -X-p covalent interaction in the octahedron gives rise to four bonding and antibonding bands along with five nonbonding bands³⁵. FA contributes one electron, Pb contributes four and I contribute five electrons per formula unit, hence, the valence electron count becomes 20. Therefore, the states up to σ_{s-p}^* are filled and the Fermi level exists in between the lower-lying Pb-s and upper-lying Pb-p antibonding bands (see Figure 1(d)). The SOC arising due to the presence of heavy element affects the band structure near the Fermi level. Figure 1(e) shows the electronic band structure of FAPbI_3 in the absence of SOC. On inclusion of SOC, the $\mathbf{L}\cdot\mathbf{S}$ coupling lifts the degeneracy between the states $\mathbf{J} = \frac{1}{2}$ and $\mathbf{J} = \frac{3}{2}$ as shown in Figure 1(f). The strength of atomic SOC is the deterministic factor towards tailoring the non-trivial topological phases in ABX_3 . However, the breaking down of the inversion symmetry causes both the atomic SOC and Rashba SOC to become deterministic

in tailoring the electronic behavior of these noncentrosymmetric quantum materials³⁶.

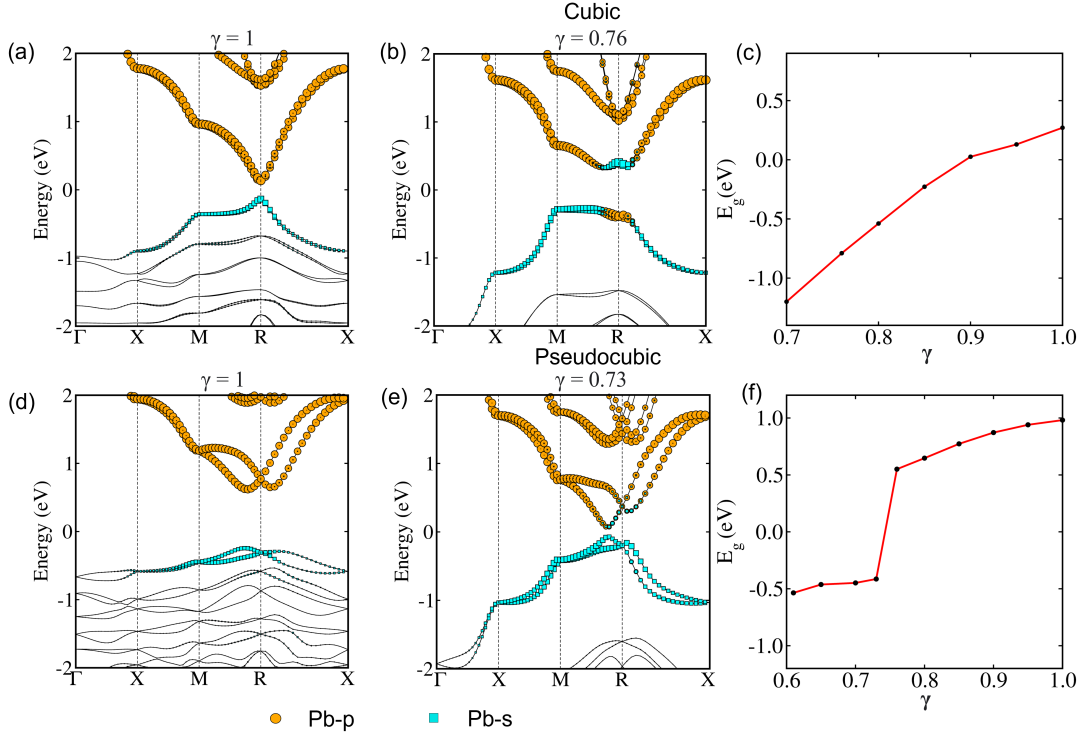


Figure 2: Orbital resolved band structure in presence of SOC for cubic and pseudocubic FAPbI₃ (a), (d) without compression, and (b), (e) at critical compression $\gamma = 0.76$, and $\gamma = 0.73$, respectively. Band gap at different values of strain in (c) cubic FAPbI₃ showing its continuous nature, and (f) pseudocubic FAPbI₃ showing a discontinuity at the critical value of strain.

The experimentally reported band gap of FAPbI₃ is 1.48 eV³⁷. The closest band gap of 1.56 eV is reproduced by $G_0W_0@HSE06+SOC$ with $\alpha=53\%$, which is in agreement with the previous report³⁸. We have observed that except for the band gaps, other band features are similar irrespective of the choice of functional (see section I of supporting information (SI)). Therefore, we have used Perdew-Burke-Ernzerhof (PBE) functional for further calculations in view of its low computational cost.

The compressional strain is a natural external stimulus to vary the bond length while maintaining the symmetry of the lattice. Therefore, we have investigated the effect of strain on the evolution of band structure. In the case of cubic FAPbI₃, at a critical compression $\gamma (V/V_0) = 0.76$, the inversion between the Pb-*s* and Pb-*p* orbital takes place. This *s-p* inversion takes place at R point and gives the initial indication of the existence of non-trivial topology under the effect of

strain. The orbital projected band structure with the orbital contribution proportional to the thickness of the symbols is shown in Figures 2(a) and (b). The continuous TPT takes place in three steps, i) shrinking ii) closing iii) reemergence of the inverted band gap, and is shown in the Figure 2(c). However, if the inversion symmetry is not preserved in a material then the nature of phase transition changes. In the case of noncentrosymmetric FAPbI₃, as we keep on increasing the strain the band gap decreases initially. But, after reaching a certain minimum value, a new negative band gap emerges with VBM and CBM inverting their orbital character. In this case, the value of this critical strain γ is 0.73 (see Figures 2(d) and (e)). This flip in the character of band structure at the critical value indicates the change in the topological nature of the material. This type of phase transition in which the gapless state is not stabilized, resulting in discontinuity in the band gap as shown in Figure 2(f), is termed a discontinuous TPT. It is also called a first-order phase transition. The distortion caused in the octahedral cage of PbI due to structural optimization is responsible for the discontinuous phase transition. Subsequently, the structural stability of cubic and pseudocubic FAPbI₃ along with the strained configurations is confirmed using *ab initio* molecular dynamics (AIMD). The radial distribution function ($g(r)$) plots at T = 0 K and T = 300 K are shown in section II of SI.

SK-TB Hamiltonian studies are useful in providing information regarding the underlying quantum mechanical process responsible for phase transition due to structural deformation³⁹. The TB model Hamiltonian in the second quantized notation is written as^{35,40}

$$H = \sum_{i,\alpha} \varepsilon_{i\alpha} c_{i\alpha}^\dagger c_{i\alpha} + \sum_{ij:\alpha\beta} t_{i\alpha,j\beta} (c_{i\alpha}^\dagger c_{j\beta} + h.c.) + \lambda \mathbf{L} \cdot \mathbf{S} + H_R. \quad (1)$$

Here, i, j and α, β represents site and orbital indices, respectively. $\varepsilon_{i\alpha}$ is the onsite energy term and $t_{i\alpha,j\beta}$ gives the hopping term. In addition to the nearest neighbor Pb-I interactions, the second neighbor Pb-Pb interactions are also included in the Hamiltonian. The third term includes SOC, where λ gives the SOC strength. H_R is included when the noncentrosymmetry is present in the crystal structure and is called Rashba SOC. $H_R = -\frac{\mu_B}{2mc} \vec{\sigma} \cdot (\vec{E} \times \vec{p})$, where \vec{E} is the electric field

experienced by the electron and $\vec{\sigma}$ is the pauli matrix vector and \vec{p} represents the momenta^{41,42}. The basis set for the TB Hamiltonian contains one Pb-*s*, three Pb-*p* and nine I-*p* orbitals. The rest orbitals are neglected as they do not participate in the formation of the topological invariant states. The spin independent Hamiltonian with the basis set in order $\langle s^{Pb} |, \langle p_x^{Pb} |, \langle p_y^{Pb} |, \langle p_z^{Pb} |, \langle p_x^{I1} |, \langle p_y^{I1} |, \langle p_z^{I1} |, \langle p_x^{I2} |, \langle p_y^{I2} |, \langle p_z^{I2} |, \langle p_x^{I3} |, \langle p_y^{I3} |, \langle p_z^{I3} |$, takes the form

$$H = \begin{pmatrix} M_{4 \times 4}^{Pb-Pb} & M_{4 \times 9}^{Pb-I} \\ (M_{4 \times 9}^{Pb-I})^\dagger & M_{9 \times 9}^{I-I} \end{pmatrix}.$$

The individual blocks of this matrix are as follows

$$M_{4 \times 4}^{Pb-Pb} = \begin{pmatrix} \epsilon_s + g_1 & 2it_{sp\sigma}^{Pb-Pb} \text{Sin}(k_x a) & 2it_{sp\sigma}^{Pb-Pb} \text{Sin}(k_y a) & 2it_{sp\sigma}^{Pb-Pb} \text{Sin}(k_z a) \\ -2it_{sp\sigma}^{Pb-Pb} \text{Sin}(k_y a) & \epsilon_{p1} + g_2 & 0 & 0 \\ -2it_{sp\sigma}^{Pb-Pb} \text{Sin}(k_x a) & 0 & \epsilon_{p1} + g_3 & 0 \\ -2it_{sp\sigma}^{Pb-Pb} \text{Sin}(k_z a) & 0 & 0 & \epsilon_{p1} + g_4 \end{pmatrix}$$

$$M_{4 \times 9}^{Pb-I} = \begin{pmatrix} t_{sp\sigma}^{Pb-I} S_x & 0 & 0 & 0 & t_{sp\sigma}^{Pb-I} S_y & 0 & 0 & 0 & t_{sp\sigma}^{Pb-I} S_z \\ t_{pp\sigma}^{Pb-I} C_x & 0 & 0 & t_{pp\pi}^{Pb-I} C_y & 0 & 0 & t_{pp\pi}^{Pb-I} C_z & 0 & 0 \\ 0 & t_{pp\pi}^{Pb-I} C_x & 0 & 0 & t_{pp\pi}^{Pb-I} C_y & 0 & 0 & t_{pp\pi}^{Pb-I} C_z & 0 \\ 0 & 0 & t_{pp\pi}^{Pb-I} C_x & 0 & 0 & t_{pp\pi}^{Pb-I} C_y & 0 & 0 & t_{pp\sigma}^{Pb-I} C_z \end{pmatrix}$$

$$M_{9 \times 9}^{I-I} = \begin{pmatrix} \varepsilon_{p2} & 0 & 0 & 0 & 0 & 0 & 0 & 0 & 0 \\ 0 & \varepsilon_{p2} & 0 & 0 & 0 & 0 & 0 & 0 & 0 \\ 0 & 0 & \varepsilon_{p2} & 0 & 0 & 0 & 0 & 0 & 0 \\ 0 & 0 & 0 & \varepsilon_{p2} & 0 & 0 & 0 & 0 & 0 \\ 0 & 0 & 0 & 0 & \varepsilon_{p2} & 0 & 0 & 0 & 0 \\ 0 & 0 & 0 & 0 & 0 & \varepsilon_{p2} & 0 & 0 & 0 \\ 0 & 0 & 0 & 0 & 0 & 0 & \varepsilon_{p2} & 0 & 0 \\ 0 & 0 & 0 & 0 & 0 & 0 & 0 & \varepsilon_{p2} & 0 \\ 0 & 0 & 0 & 0 & 0 & 0 & 0 & 0 & \varepsilon_{p2} \end{pmatrix}.$$

Here ε_s , ε_{p1} , and ε_{p2} are the onsite energies of Pb-s, Pb-p and I-p orbitals, respectively. The terms C_z and S_z are the representations for $2\cos(k_z a/2)$ and $2i\sin(k_z a/2)$, and g_i ($i = 1,2,3,4$) are the \mathbf{k} -dependent hopping integrals arising from the Pb-Pb second neighbor interactions given by

$$\begin{aligned} g_1 &= 2t_{ss}^{Pb-Pb} [\cos(k_x a) + \cos(k_y a) + \cos(k_z a)], \\ g_2 &= 2t_{pp\sigma}^{Pb-Pb} \cos(k_x a) + 2t_{pp\pi}^{Pb-Pb} [\cos(k_y a) + \cos(k_z a)], \\ g_3 &= 2t_{pp\sigma}^{Pb-Pb} \cos(k_y a) + 2t_{pp\pi}^{Pb-Pb} [\cos(k_x a) + \cos(k_z a)], \\ g_4 &= 2t_{pp\sigma}^{Pb-Pb} \cos(k_z a) + 2t_{pp\pi}^{Pb-Pb} [\cos(k_x a) + \cos(k_y a)]. \end{aligned}$$

The SOC component of the Hamiltonian is obtained by applying $\lambda \mathbf{L} \cdot \mathbf{S}$ on the Pb-p states, as Pb being heavy is responsible for the SOC. We have obtained the matrix elements for the SOC Hamiltonian with the basis set in the order: $|p_x^{Pb} \uparrow\rangle$, $|p_y^{Pb} \uparrow\rangle$, $|p_z^{Pb} \uparrow\rangle$, $|p_x^{Pb} \downarrow\rangle$, $|p_y^{Pb} \downarrow\rangle$, $|p_z^{Pb} \downarrow\rangle$

$$H_{SOC} = \lambda \begin{pmatrix} 0 & -i & 0 & 0 & 0 & 1 \\ i & 0 & 0 & 0 & 0 & -i \\ 0 & 0 & 0 & 1 & -i & 0 \\ 0 & 0 & 1 & 0 & i & 0 \\ 0 & 0 & i & -i & 0 & 0 \\ 1 & i & 0 & 0 & 0 & 0 \end{pmatrix}.$$

Table 1: Interaction parameters and SOC strength for FAPbI₃ from thirteen band hamiltonian at zero and critical compression strength in units of eV.

Type	E_{Pb-s}	E_{Pb-p}	E_{I-p}	$t_{sp\sigma}^{Pb-I}$	$t_{pp\sigma}^{Pb-I}$	$t_{pp\pi}^{Pb-I}$	$t_{ss\sigma}^{Pb-Pb}$	$t_{sp\sigma}^{Pb-Pb}$	$t_{pp\sigma}^{Pb-Pb}$	$t_{pp\pi}^{Pb-Pb}$	λ
Cubic ($\gamma = 1$)	-1	2.5	-2	0.15	0.4	0.3	-0.1	0.3	0.4	0.1	0.5
Cubic ($\gamma = 0.76$)	-1	2.5	-2	0.1	0.7	0.5	-0.1	0.3	0.76	0.17	0.5
Pseudocubic ($\gamma = 1$)	-0.8	3	-1	0.15	0.4	0.3	-0.07	0.45	0.5	0.4	0.4
Pseudocubic ($\gamma = 0.73$)	-1	3	-2	0.1	0.5	0.5	-0.11	0.5	0.95	0.07	0.4

Fitting this thirteen band model with the DFT bands, we get the effective onsite and hopping terms. The parameters obtained at no strain and critical strain are provided in Table 1. In the case of FAPbI₃, the bands forming the VBM and CBM are primarily composed of Pb- $\{s,p\}$ orbitals. Also, the band inversion is taking place between Pb- s , and Pb- p orbitals. Therefore, a minimal basis Hamiltonian containing only essential interactions have been developed. The second neighbor Pb-Pb interactions has been considered in formulating the four band model. The SOC incorporated four band Hamiltonian is written as

$$\mathbf{H} = \begin{pmatrix} H_{\uparrow\uparrow} & H_{\uparrow\downarrow} \\ H_{\downarrow\uparrow} & H_{\downarrow\downarrow} \end{pmatrix}$$

where

$$H_{\uparrow\downarrow} = \begin{pmatrix} 0 & 0 & 0 & 0 \\ 0 & 0 & 0 & \lambda \\ 0 & 0 & 0 & -i\lambda \\ 0 & 0 & \lambda & -i\lambda \end{pmatrix}$$

$$H_{\uparrow\uparrow} = \begin{pmatrix} \epsilon_s + g_1 & 2it_{sp\sigma}^{Pb-Pb} \text{Sin}(k_x a) & 2it_{sp\sigma}^{Pb-Pb} \text{Sin}(k_y a) & 2it_{sp\sigma}^{Pb-Pb} \text{Sin}(k_z a) \\ -2it_{sp\sigma}^{Pb-Pb} \text{Sin}(k_y a) & \epsilon_{p1} + g_2 & 0 & 0 \\ -2it_{sp\sigma}^{Pb-Pb} \text{Sin}(k_x a) & 0 & \epsilon_{p1} + g_3 & 0 \\ -2it_{sp\sigma}^{Pb-Pb} \text{Sin}(k_z a) & 0 & 0 & \epsilon_{p1} + g_4 \end{pmatrix}$$

Table 2: Interaction parameters and SOC strength for FAPbI₃ from four band hamiltonian at zero and critical compression strength in units of eV.

Type	E_{pb-s}	E_{pb-p}	$t_{ss\sigma}^{Pb-Pb}$	$t_{sp\sigma}^{Pb-Pb}$	$t_{pp\sigma}^{Pb-Pb}$	$t_{pp\pi}^{Pb-Pb}$	λ
Cubic ($\gamma = 1$)	-0.8	2.5	-0.09	0.3	0.4	0.1	0.5
Cubic ($\gamma = 0.76$)	-1.2	2.5	-0.19	0.44	0.75	0.16	0.5
Pseudocubic ($\gamma = 1$)	-0.8	2.5	-0.1	0.25	0.2	0.06	0.5
Pseudocubic ($\gamma = 0.73$)	-1	3	-0.12	0.4	0.8	0.1	0.5

The interaction parameters for both cubic and pseudocubic FAPbI₃, from the four band model fitting are provided in Table 2. Magnitude of all the parameters increase with rise in strain. With the increase in compression, the bond length decreases and hence the strength of interactions increases. In comparison to Pb-Pb $ss\sigma$, $sp\sigma$ and $pp\pi$, the $pp\sigma$ interactions are most sensitive to the strain. For cubic structure the $pp\sigma$ interaction rises from 0.4 to 0.75, while for pseudocubic, it rises from 0.2 to 0.7, upon the application of respective critical strain. We have also observed that λ does not change with compression, therefore, SOC is insensitive to the strain. From the electronic band structure calculations, it is evident that the universality of the band structure arises from the nearest-neighbor Pb- $\{s,p\}$ -X- p covalent interactions. However, the TB model elucidates that the

second neighbor Pb- $\{s,p\}$ -Pb- $\{s,p\}$ interactions act as a driving force for band gap engineering and non-trivial phases. This type of TB model is universal, as it is independent of the choice of functional adopted³⁵.

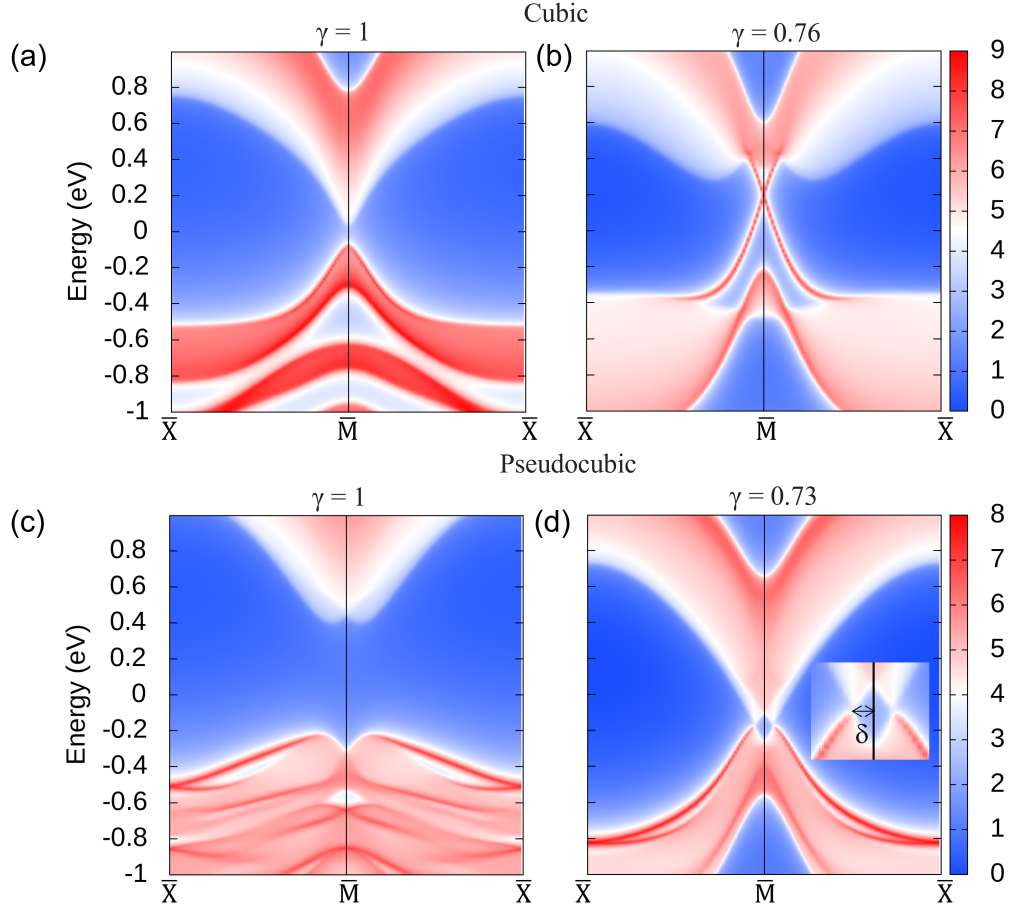


Figure 3: Surface band structure in presence of SOC for cubic FAPbI₃ (a) without compression, (b) at critical compression $\gamma = 0.76$, and pseudocubic FAPbI₃ (c) without compression, (d) at critical compression $\gamma = 0.73$.

The study of bulk electronic structure has enabled us to identify the possibility of non-trivial topology and phase transition in halide perovskites. However, the practical observation of these states comes from the calculation of surface states⁴³. The DFT based calculations on the slab structure require a huge amount of computational time and memory to analyze these properties. So, we have used the maximally localized wannier function (MLWF) based TB approach to construct a semi-infinite slab along (001) direction, minimizing the total spread of MLWF. As expected,

there is an absence of the surface states in FAPbI₃ at ambient conditions (see Figures 3(a) and (c)). However, as the critical value of strain i.e., $\gamma = 0.76$ is applied to cubic FAPbI₃, the conducting states are formed at \bar{M} point, similar to that of a conventional topological insulator. The invariant surface states, exhibited by cubic FAPbI₃ yields two interpenetrating Dirac states. In this case, the Kramer pair i.e., doubly degenerate dirac cones, each one arising from the VB and CB coincides at \bar{M} point (see Figure 3(b)). But when the inversion symmetry is broken, this degeneracy is lifted and as a result one cone shifts towards the VB and the other towards the CB¹⁹. Therefore, we see two Dirac states at $\bar{M} \pm \delta$, along the path $X-\bar{M}-X$, as shown in Figure 3(d). The resulting surface states illustrate the presence of discontinuous nature of NI-TI TPT.

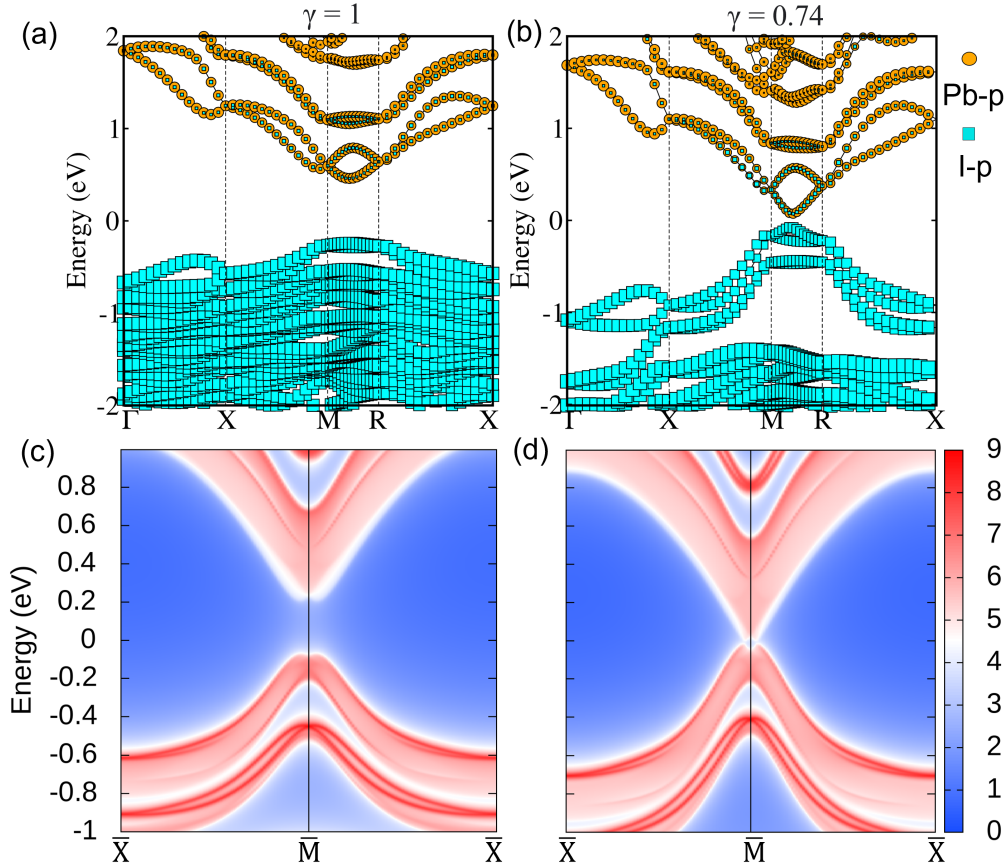


Figure 4: Orbital resolved band structure in presence of SOC for Cs_{0.5}MA_{0.5}PbI₃ (a) without compression, (b) at critical compression $\gamma = 0.74$. Surface band structure for Cs_{0.5}MA_{0.5}PbI₃ (a) without compression, (b) at critical compression $\gamma = 0.74$.

We have studied the TPT in both inorganic (CsPbI₃) and organic (MAPbI₃, FAPbI₃) halide

perovskites. CsPbI₃ show continuous TPT at $\gamma = 0.76$ because of its centrosymmetric nature, whereas MAPbI₃ and FAPbI₃ show similar behaviour (see section III and IV of SI for CsPbI₃ and MAPbI₃, respectively). It has been found that by partially replacing MA⁺ with Cs⁺, the stability can be enhanced in ambient environment⁴⁴. These mixed cation/anion perovskites have attracted considerable attention due to their higher stability⁴⁵. Thus, we have designed the mixed cation halide perovskites to study the nature of TPT in them. For this, three configurations i.e., Cs_{0.75}MA_{0.5}PbI₃, Cs_{0.5}MA_{0.5}PbI₃, Cs_{0.25}MA_{0.75}PbI₃, have been obtained by replacing MA with Cs in the lattice of MAPbI₃ (see section V of SI for crystal structures). Firstly, we have calculated the thermodynamic stability of the mixed cation halide perovskites i.e., Cs_{0.75}MA_{0.5}PbI₃, Cs_{0.5}MA_{0.5}PbI₃, Cs_{0.25}MA_{0.75}PbI₃. The precursors considered for the calculation of formation energy (E_f) of these perovskites are MAPbI₃, CsI and PbI₂. The associated expression is

$$E_f(x,y) = E_{sys} - E(MA_4Pb_4I_{12}) - xE(CsI) - yE(PbI_2) \quad (2)$$

Here, coefficients x and y of each term on the right hand side are chosen such that they stoichiometrically balance the equation. $1 \times 2 \times 2$ supercell of MAPbI₃ has been used. $E_f(x,y)$ for Cs_{0.75}MA_{0.25}PbI₃, Cs_{0.5}MA_{0.5}PbI₃, Cs_{0.25}MA_{0.75}PbI₃ is -0.78 eV, -0.69 eV and -0.65 eV, respectively. The negative formation energy shows that all the configurations are thermodynamically stable. We have also checked the structural stability of these configurations using AIMD simulations (see section V of SI). After this, we have obtained the band structure for all the configurations with and without SOC. When no strain is applied in Cs_{0.5}MA_{0.5}PbI₃, the VBM is composed of I- p orbitals, and CBM of Pb- p orbitals (see Figure 4(a)). The inclusion of SOC does not depict any traits of non-trivial topological nature. Subsequently, we have applied the compressional volumetric strain along with the SOC. At the critical strain value of $\gamma = 0.74$, the appearance of a negative band gap is observed with the inverted orbital character as seen in Figure 4(b). This suggests the possibility of TPT in Cs_{0.5}MA_{0.5}PbI₃. Whereas, in Cs_{0.75}MA_{0.25}PbI₃ and Cs_{0.25}MA_{0.75}PbI₃, no such parity inversion is observed under the effect of compression. This may be attributed to the difference in the ionic radii of Cs and MA cations, which is 1.88 Å and 2.117 Å, respectively. As

the band inversion involves p orbitals of both I and Pb, therefore, a four band TB model will not suffice in predicting the nature of TPT. Thus, using the thirteen band model containing Pb- $\{s,p\}$ and X- p orbitals, we have calculated the onsite energies and hopping integrals (see section VI of SI). All the interaction parameters increase on application of strain, but the Pb-I $pp\pi$ interactions rising from 1 to 1.5 are most affected by the same. After this, we have plotted the surface state band structure for $\text{Cs}_{0.5}\text{MA}_{0.5}\text{PbI}_3$ at $\gamma = 0$ and $\gamma = 0.74$. As seen in the Figures 4(b) and (c), the origin of surface states with strain confirms the TPT at $\gamma = 0.74$.

The strain free lead halide perovskites are trivial band insulators, however, a TPT can take place via strain engineering. The presence of inversion symmetry plays a vital role in the electronic properties of the halide perovskites. The first-principles calculations suggest that FAPbI_3 becomes noncentrosymmetric on structural optimization. The centrosymmetric FAPbI_3 shows a continuous phase transition on the application of strain. The inversion symmetry breaking changes the nature of this quantum phase transition. At a critical value of $\gamma = 0.73$, pseudocubic FAPbI_3 undergoes a first-order TPT. The discontinuity is evident from the band gaps calculated at various values of strain, and the nature of surface states. This study also shows that although thirteen orbitals participate in the chemical bonding, a four band TB model is sufficient to capture energy dispersion near the Fermi level. The Pb-Pb second neighbor interactions determine the topology of this class of materials. The Pb-Pb $pp\sigma$ interactions are the most affected by the application of strain. Hence, these interactions are the driving forces in determining the phase transition. Furthermore, the mixed cation perovskites $\text{Cs}_{0.75}\text{MA}_{0.25}\text{PbI}_3$, $\text{Cs}_{0.5}\text{MA}_{0.5}\text{PbI}_3$ and $\text{Cs}_{0.25}\text{MA}_{0.75}\text{PbI}_3$ are thermodynamically and structurally stable. $\text{Cs}_{0.5}\text{MA}_{0.5}\text{PbI}_3$ shows TPT at a compression of $\gamma = 0.74$, which is shown by band inversion and the nature of surface states. The structural stability of these perovskites under strain strengthens that these phase transitions can be realized experimentally.

Computational Methods

The calculations are performed using DFT^{46,47} with the Projected Augmented Wave (PAW)^{48,49} method implemented in Vienna *Ab initio* Simulation Package (VASP)⁵⁰ code. The self-consistent relativistic calculations are performed using the Generalized Gradient Approximation (GGA) of PBE⁵¹. The structural parameters are fully optimized until the Hellmann-Feynman forces are smaller than 1 meV/Å. The cutoff energy of 520 eV is used for the plane wave basis set such that the total energy calculations are converged within 10^{-5} eV. A Γ -centered $4 \times 4 \times 4$ k -grid is used to sample the irreducible BZ of cubic phase with the $Pm\bar{3}m$ space group. Throughout the calculations, we have included SOC in order to consider the relativistic effects due to the presence of heavy element in the systems. We have used many-body perturbation method $G_0W_0@HSE06+SOC$ for the better estimation of the band gap⁵². For this, the number of bands is set to six times the number of occupied bands. After this, to investigate the topological phases, the first-principles calculations were first performed using fully relativistic norm-conserving pseudopotentials as implemented in the QUANTUM ESPRESSO code⁵³. The results of these DFT calculations are then fed as input to WANNIER90⁵⁴ for constructing a TB model based on Maximally Localized Wannier Functions (MLWFs) with p orbitals of I and sp orbitals Pb. The surface states are then calculated using the Green's function through an interactive method as implemented in the Wannier-TOOLS package⁵⁵. A TB model using Slater and Koster approach is constructed in the two-center approximation using the package Tight Binding Studio⁵⁶. A nonlinear fitting algorithm is used to find the best fit entries for both Hamiltonian and overlap matrices to reproduce the first-principles data. Finally, the structural stability of different configurations is checked at higher temperature using AIMD by running a 5 ps long simulation with NVT ensemble (Nose–Hoover thermostat).

Acknowledgement

A.P. acknowledges IIT Delhi for the senior research fellowship. S.S. acknowledges CSIR, India, for the senior research fellowship [grant no. 09/086(1432)/2019-EMR-I]. S.B. acknowledges fi-

nancial support from SERB under a core research grant (grant no. CRG/2019/000647) to set up his High Performance Computing (HPC) facility “Veena” at IIT Delhi for computational resources.

Supporting Information Available

Band profile of FAPbI₃ using PBE+SOC and G₀W₀@HSE06+SOC ϵ_{xc} functionals; Structural stability of cubic and pseudocubic FAPbI₃; Continuous TPT in cubic CsPbI₃; TPT in cubic and pseudocubic MAPbI₃; Crystal structures and structural stability of Cs_{0.5}MA_{0.5}PbI₃, Cs_{0.75}MA_{0.25}PbI₃ and Cs_{0.25}MA_{0.75}PbI₃; TB parameters for Cs_{0.5}MA_{0.5}PbI₃.

References

- (1) Bansil, A.; Lin, H.; Das, T. Colloquium: Topological band theory. *Rev. Mod. Phys.* **2016**, *88*, 021004.
- (2) Wang, Z.; Sun, Y.; Chen, X.-Q.; Franchini, C.; Xu, G.; Weng, H.; Dai, X.; Fang, Z. Dirac semimetal and topological phase transitions in A₃Bi (A= Na, K, Rb). *Phys. Rev. B* **2012**, *85*, 195320.
- (3) Wang, Z.; Weng, H.; Wu, Q.; Dai, X.; Fang, Z. Three-dimensional Dirac semimetal and quantum transport in Cd₃As₂. *Phys. Rev. B* **2013**, *88*, 125427.
- (4) Wan, X.; Turner, A. M.; Vishwanath, A.; Savrasov, S. Y. Topological semimetal and Fermi-arc surface states in the electronic structure of pyrochlore iridates. *Phys. Rev. B* **2011**, *83*, 205101.
- (5) Xu, S.-Y.; Belopolski, I.; Alidoust, N.; Neupane, M.; Bian, G.; Zhang, C.; Sankar, R.; Chang, G.; Yuan, Z.; Lee, C.-C. et al. Discovery of a Weyl fermion semimetal and topological Fermi arcs. *Science* **2015**, *349*, 613–617.
- (6) Burkov, A. Topological semimetals. *Nat. Mater.* **2016**, *15*, 1145–1148.

- (7) Fu, L. Topological crystalline insulators. *Phys. Rev. Lett.* **2011**, *106*, 106802.
- (8) Hor, Y.; Richardella, A.; Roushan, P.; Xia, Y.; Checkelsky, J.; Yazdani, A.; Hasan, M.; Ong, N.; Cava, R. p-type Bi_2Se_3 for topological insulator and low-temperature thermoelectric applications. *Phys. Rev. B* **2009**, *79*, 195208.
- (9) Xu, Y.; Gan, Z.; Zhang, S.-C. Enhanced thermoelectric performance and anomalous Seebeck effects in topological insulators. *Phys. Rev. Lett.* **2014**, *112*, 226801.
- (10) Pal, K.; Anand, S.; Waghmare, U. V. Thermoelectric properties of materials with nontrivial electronic topology. *J Mat. Chem. C* **2015**, *3*, 12130–12139.
- (11) Zhang, H.; Liu, C.-X.; Qi, X.-L.; Dai, X.; Fang, Z.; Zhang, S.-C. Topological insulators in Bi_2Se_3 , Bi_2Te_3 and Sb_2Te_3 with a single Dirac cone on the surface. *Nat. Phys.* **2009**, *5*, 438–442.
- (12) Park, K.; Heremans, J.; Scarola, V.; Minic, D. Robustness of topologically protected surface states in layering of Bi_2Te_3 thin films. *Phys. Rev. Lett.* **2010**, *105*, 186801.
- (13) Yang, M.; Liu, W.-M. The dp band-inversion topological insulator in bismuth-based skutterudites. *Sci. Rep.* **2014**, *4*, 1–7.
- (14) Xiao, D.; Yao, Y.; Feng, W.; Wen, J.; Zhu, W.; Chen, X.-Q.; Stocks, G. M.; Zhang, Z. Half-Heusler compounds as a new class of three-dimensional topological insulators. *Phys. Rev. Lett.* **2010**, *105*, 096404.
- (15) Feng, W.; Xiao, D.; Zhang, Y.; Yao, Y. Half-Heusler topological insulators: A first-principles study with the Tran-Blaha modified Becke-Johnson density functional. *Phys. Rev. B* **2010**, *82*, 235121.
- (16) Yan, B.; Jansen, M.; Felser, C. A large-energy-gap oxide topological insulator based on the superconductor BaBiO_3 . *Nat. Phys.* **2013**, *9*, 709–711.

- (17) Li, G.; Yan, B.; Thomale, R.; Hanke, W. Topological nature and the multiple Dirac cones hidden in Bismuth high-Tc superconductors. *Sci. Rep.* **2015**, *5*, 1–8.
- (18) Khamari, B.; Kashikar, R.; Nanda, B. Topologically invariant double Dirac states in bismuth-based perovskites: Consequence of ambivalent charge states and covalent bonding. *Phys. Rev. B* **2018**, *97*, 045149.
- (19) Kore, A.; Kashikar, R.; Gupta, M.; Singh, P.; Nanda, B. Pressure and inversion symmetry breaking field-driven first-order phase transition and formation of Dirac circle in perovskites. *Phys. Rev. B* **2020**, *102*, 035116.
- (20) Jain, M.; Gill, D.; Bhumla, P.; Basera, P.; Bhattacharya, S. Theoretical insights to excitonic effect in lead bromide perovskites. *Appl. Phys. Lett.* **2021**, *118*, 192103.
- (21) Jain, M.; Singh, A.; Basera, P.; Kumar, M.; Bhattacharya, S. Understanding the role of Sn substitution and $\text{Pb}_{1-x-y}\text{Sn}_x\text{Br}_3$ in enhancing the optical properties and solar cell efficiency of $\text{CH}(\text{NH}_2)_2\text{Pb}_{1-x-y}\text{Sn}_x\text{Br}_3$. *J. Mater. Chem. C* **2020**, *8*, 10362–10368.
- (22) Jain, M.; Gill, D.; Monga, S.; Bhattacharya, S. Theoretical evaluation of oxynitride, oxyfluoride and nitrofluoride perovskites with promising photon absorption properties for solar water splitting. *arXiv preprint arXiv:2301.04335* **2023**,
- (23) Bhumla, P.; Jain, M.; Sheoran, S.; Bhattacharya, S. Vacancy-Ordered Double Perovskites Cs_2BI_6 (B= Pt, Pd, Te, Sn): An Emerging Class of Thermoelectric Materials. *J. Phys. Chem. Lett.* **2022**, *13*, 11655–11662.
- (24) Yang, K.; Setyawan, W.; Wang, S.; Buongiorno Nardelli, M.; Curtarolo, S. A search model for topological insulators with high-throughput robustness descriptors. *Nat. Mater.* **2012**, *11*, 614–619.
- (25) Kashikar, R.; Khamari, B.; Nanda, B. Second-neighbor electron hopping and pressure in-

- duced topological quantum phase transition in insulating cubic perovskites. *Phys. Rev. Mater.* **2018**, *2*, 124204.
- (26) Kashikar, R.; Gupta, M.; Nanda, B. Defining the topological influencers and predictive principles to engineer the band structure of halide perovskites. *Phys. Rev. B* **2020**, *101*, 155102.
- (27) Jin, H.; Im, J.; Freeman, A. J. Topological insulator phase in halide perovskite structures. *Phys. Rev. B* **2012**, *86*, 121102.
- (28) Krizman, G.; Assaf, B.; Phuphachong, T.; Bauer, G.; Springholz, G.; de Vaulchier, L.; Guldner, Y. Dirac parameters and topological phase diagram of $\text{Pb}_{1-x}\text{Sn}_x\text{Se}$ from magnetospectroscopy. *Phys. Rev. B* **2018**, *98*, 245202.
- (29) Wojek, B. M.; Dziawa, P.; Kowalski, B.; Szczerbakow, A.; Black-Schaffer, A. M.; Berntsen, M.; Balasubramanian, T.; Story, T.; Tjernberg, O. Band inversion and the topological phase transition in $(\text{Pb},\text{Sn})\text{Se}$. *Phys. Rev. B* **2014**, *90*, 161202.
- (30) Juričić, V.; Abergel, D. S.; Balatsky, A. V. First-order quantum phase transition in three-dimensional topological band insulators. *Phys. Rev. B* **2017**, *95*, 161403.
- (31) Zeljkovic, I.; Okada, Y.; Serbyn, M.; Sankar, R.; Walkup, D.; Zhou, W.; Liu, J.; Chang, G.; Wang, Y. J.; Hasan, M. Z. et al. Dirac mass generation from crystal symmetry breaking on the surfaces of topological crystalline insulators. *Nat. Mater.* **2015**, *14*, 318–324.
- (32) Weller, M. T.; Weber, O. J.; Frost, J. M.; Walsh, A. Cubic perovskite structure of black formamidinium lead iodide, $\alpha\text{-}[\text{HC}(\text{NH}_2)_2]\text{PbI}_3$, at 298 K. *J. Phys. Chem. Lett.* **2015**, *6*, 3209–3212.
- (33) Banerjee, A.; Chakraborty, S.; Ahuja, R. Rashba Triggered Electronic and Optical Properties Tuning in Mixed Cation–Mixed Halide Hybrid Perovskites. *ACS Appl. Energy Mater.* **2019**, *2*, 6990–6997.

- (34) Wang, S.; Xiao, W.-b.; Wang, F. Structural, electronic, and optical properties of cubic formamidinium lead iodide perovskite: A first-principles investigation. *RSC Adv.* **2020**, *10*, 32364–32369.
- (35) Kashikar, R.; Gupta, M.; Nanda, B. A generic Slater–Koster description of the electronic structure of centrosymmetric halide perovskites. *J Chem. Phys.* **2021**, *154*, 104706.
- (36) Frohna, K.; Deshpande, T.; Harter, J.; Peng, W.; Barker, B. A.; Neaton, J. B.; Louie, S. G.; Bakr, O. M.; Hsieh, D.; Bernardi, M. Inversion symmetry and bulk Rashba effect in methylammonium lead iodide perovskite single crystals. *Nat. Commun.* **2018**, *9*, 1–9.
- (37) Aharon, S.; Dymshits, A.; Rotem, A.; Etgar, L. Temperature dependence of hole conductor free formamidinium lead iodide perovskite based solar cells. *J. Mater. Chem. A* **2015**, *3*, 9171–9178.
- (38) Basera, P.; Singh, A.; Gill, D.; Bhattacharya, S. Capturing excitonic and polaronic effects in lead iodide perovskites using many-body perturbation theory. *J Mater. Chem. C* **2021**, *9*, 17113–17123.
- (39) Boyer-Richard, S.; Katan, C.; Traore, B.; Scholz, R.; Jancu, J.-M.; Even, J. Symmetry-based tight binding modeling of halide perovskite semiconductors. *J. Phys. Chem. Lett.* **2016**, *7*, 3833–3840.
- (40) Do, T.-N.; Shih, P.-H.; Lin, H.; Huang, D.; Gumbs, G.; Chang, T.-R. Generalized Peierls substitution for the tight-binding model of twisted graphene systems in a magnetic field. *Phys. Rev. B* **2022**, *105*, 235418.
- (41) Sheoran, S.; Kumar, M.; Bhumla, P.; Bhattacharya, S. Rashba spin splitting and anomalous spin textures in the bulk ferroelectric oxide perovskite KIO_3 . *Mater. Adv.* **2022**,
- (42) Sheoran, S.; Bhumla, P.; Bhattacharya, S. Emergence of cubic ordered full-plane persistent spin textures in lead-free materials. *Phys. Rev. Mater.* **2022**, *6*, 094602.

- (43) Phutela, A.; Bhumla, P.; Jain, M.; Bhattacharya, S. Exploring strong and weak topological states on isostructural substitutions in TlBiSe_2 . *arXiv preprint arXiv:2205.08950* **2022**,
- (44) Ma, X.-X.; Li, Z.-S. Substituting Cs for MA on the surface of MAPbI_3 perovskite: A first-principles study. *Comput. Mater. Sci.* **2018**, *150*, 411–417.
- (45) Gao, W.; Ran, C.; Li, J.; Dong, H.; Jiao, B.; Zhang, L.; Lan, X.; Hou, X.; Wu, Z. Robust stability of efficient lead-free formamidinium tin iodide perovskite solar cells realized by structural regulation. *J. Phys. Chem. Lett.* **2018**, *9*, 6999–7006.
- (46) Hohenberg, P.; Kohn, W. Inhomogeneous electron gas. *Phys. Rev.* **1964**, *136*, B864.
- (47) Kohn, W.; Sham, L. J. Self-consistent equations including exchange and correlation effects. *Phys. Rev.* **1965**, *140*, A1133.
- (48) Kresse, G.; Joubert, D. From ultrasoft pseudopotentials to the projector augmented-wave method. *Phys. Rev. B* **1999**, *59*, 1758.
- (49) Blöchl, P. E. Projector augmented-wave method. *Phys. Rev. B* **1994**, *50*, 17953.
- (50) Kresse, G.; Furthmüller, J. Efficient iterative schemes for ab initio total-energy calculations using a plane-wave basis set. *Phys. Rev. B* **1996**, *54*, 11169.
- (51) Perdew, J. P.; Burke, K.; Ernzerhof, M. Generalized gradient approximation made simple. *Phys. Rev. Lett.* **1996**, *77*, 3865.
- (52) Hedin, L. New method for calculating the one-particle Green's function with application to the electron-gas problem. *Phys. Rev.* **1965**, *139*, A796.
- (53) Giannozzi, P.; Baroni, S.; Bonini, N.; Calandra, M.; Car, R.; Cavazzoni, C.; Ceresoli, D.; Chiarotti, G. L.; Cococcioni, M.; Dabo, I. QUANTUM ESPRESSO: a modular and open-source software project for quantum simulations of materials. *J. Phys.: Condens. Matter* **2009**, *21*, 395502.

- (54) Mostofi, A. A.; Yates, J. R.; Lee, Y.-S.; Souza, I.; Vanderbilt, D.; Marzari, N. wannier90: A tool for obtaining maximally-localised Wannier functions. *Comput. Phys. Commun.* **2008**, *178*, 685–699.
- (55) Wu, Q.; Zhang, S.; Song, H.-F.; Troyer, M.; Soluyanov, A. A. WannierTools: An open-source software package for novel topological materials. *Comput. Phys. Commun.* **2018**, *224*, 405–416.
- (56) Nakhace, M.; Ketabi, S. A.; Peeters, F. M. Tight-binding studio: A technical software package to find the parameters of tight-binding Hamiltonian. *Comput. Phys. Commun* **2020**, *254*, 107379.

Strain-driven topological quantum phase transition in the family of halide perovskites

Ankita Phutela,* Sajjan Shoeran, and Saswata Bhattacharya*

Department of Physics, Indian Institute of Technology Delhi, New Delhi, India

E-mail: Ankita@physics.iitd.ac.in[AP]; saswata@physics.iitd.ac.in[SB]

Phone: +91-11-2659 1359. Fax: +91-11-2658 2037

Supplementary Information

- I.** Band profile of FAPbI_3 using PBE+SOC and G_0W_0 @HSE06+SOC ϵ_{xc} functionals.
- II.** Structural stability of cubic and pseudocubic FAPbI_3 .
- III.** Continuous TPT in cubic CsPbI_3 .
- IV.** TPT in cubic and pseudocubic MAPbI_3 .
- V.** Crystal structures and structural stability of $\text{Cs}_{0.5}\text{MA}_{0.5}\text{PbI}_3$, $\text{Cs}_{0.75}\text{MA}_{0.25}\text{PbI}_3$ and $\text{Cs}_{0.25}\text{MA}_{0.75}\text{PbI}_3$.
- VI.** TB parameters for $\text{Cs}_{0.5}\text{MA}_{0.5}\text{PbI}_3$.

Band profile of FAPbI_3 using PBE+SOC and $\text{G}_0\text{W}_0\text{@HSE06+SOC}$ ϵ_{xc} functionals.

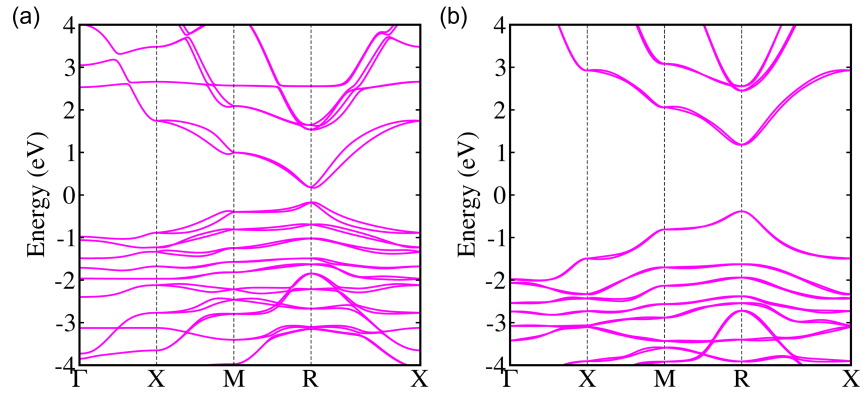


Figure S1: Band structure of FAPbI_3 calculated using (a) PBE+SOC and (b) $\text{G}_0\text{W}_0\text{@HSE06+SOC}$.

Structural stability of cubic and pseudocubic FAPbI_3 .

We have checked the structural stability of cubic and pseudocubic FAPbI_3 along with the strained configurations using *ab initio* molecular dynamics (AIMD). For this, we have obtained the radial distribution function ($g(r)$) at $T = 0\text{K}$ and $T = 300\text{K}$. We have observed that the nature of radial distribution function remains the same at room temperature for the nearest neighbors (see Figure S2). Therefore, we validate that the configurations are structurally stable at 300K even after undergoing compression. This makes them useful in realizing the practical applications.

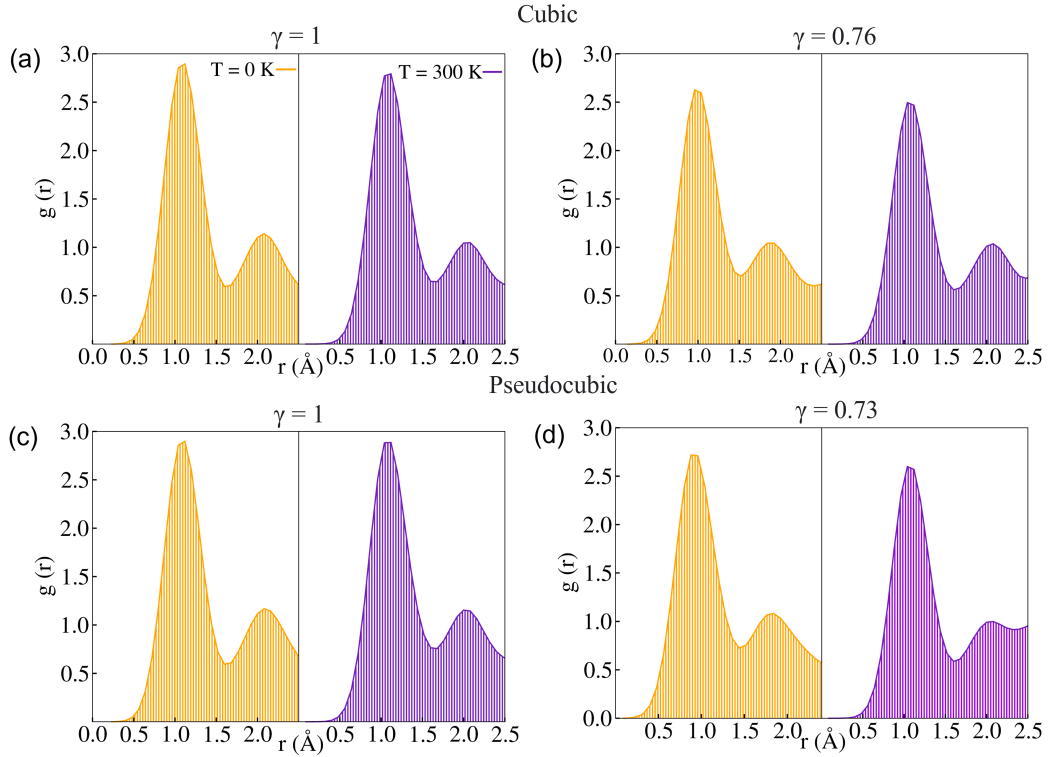


Figure S2: Radial distribution function for different phases of FAPbI_3 namely (a) cubic, (b) strained cubic ($\gamma = 0.76$), (c) pseudocubic and (d) strained pseudocubic ($\gamma = 0.73$) at $T = 0\text{K}$ and $T = 300\text{K}$.

Continuous TPT in cubic CsPbI₃.

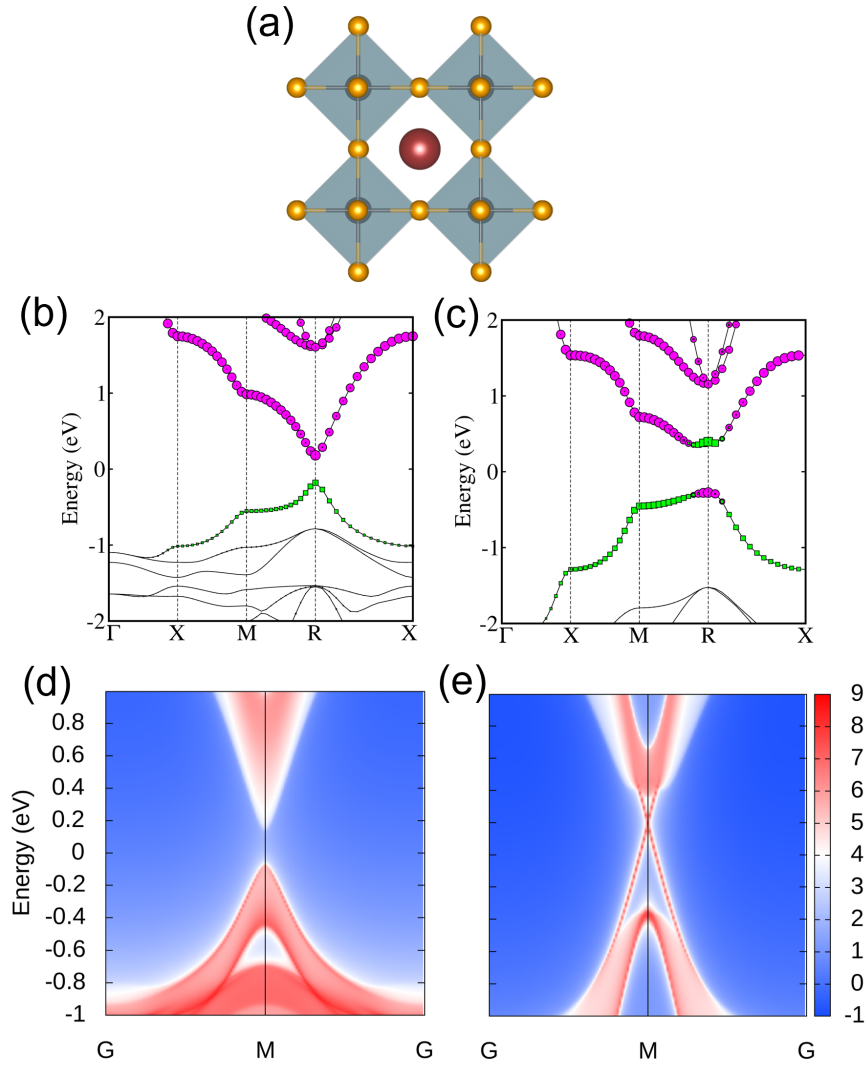


Figure S3: (a) Crystal structure of cubic CsPbI₃. Bulk band structure (b) without compression with Pb-*p* (magenta) contribution at CBM and Pb-*s* (green) contribution at VBM, and (c) with compression $\gamma = 0.76$, showing band inversion at R point. Surface band structure (d) without, and (e) with compression, showing a continuous transition from normal to topological state.

TPT in cubic and pseudocubic MAPbI₃.

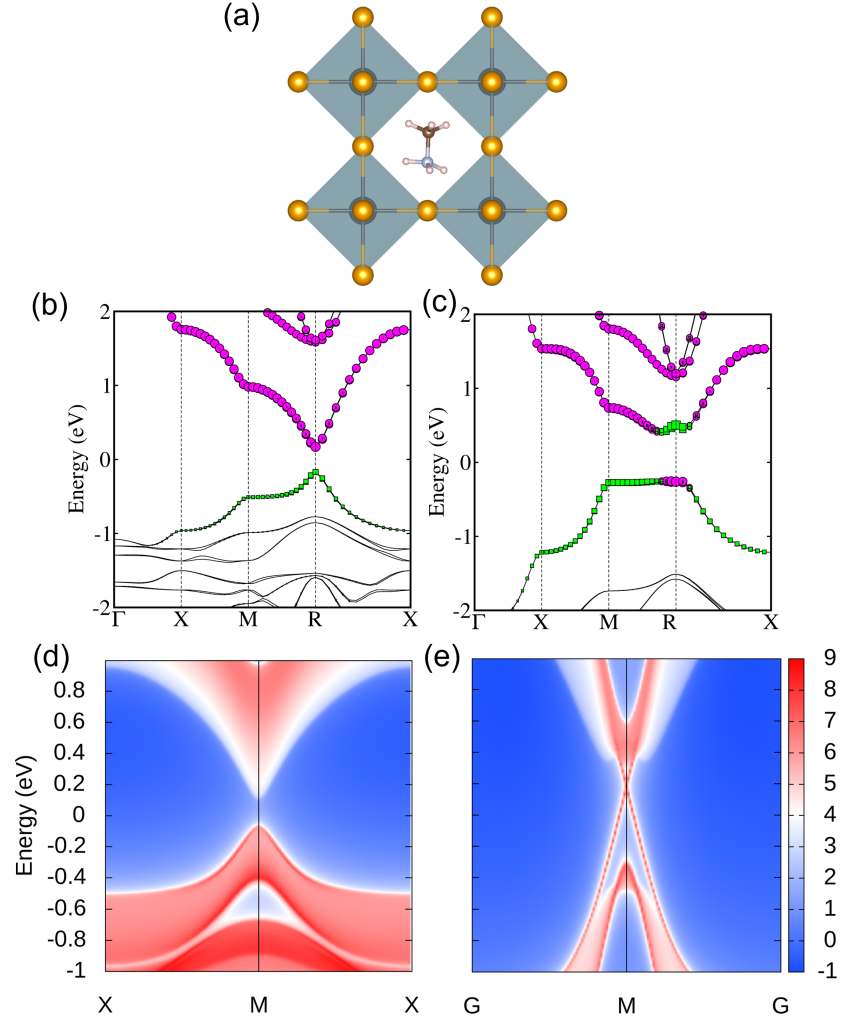


Figure S4: (a) Crystal structure of cubic MAPbI₃. Bulk band structure (b) without compression with Pb-*p* (magenta) contribution at CBM and Pb-*s* (green) contribution at VBM, and (c) with compression $\gamma = 0.73$, showing band inversion at R point. Surface band structure (d) without, and (e) with compression $\gamma = 0.73$, showing a continuous transition from normal to topological state.

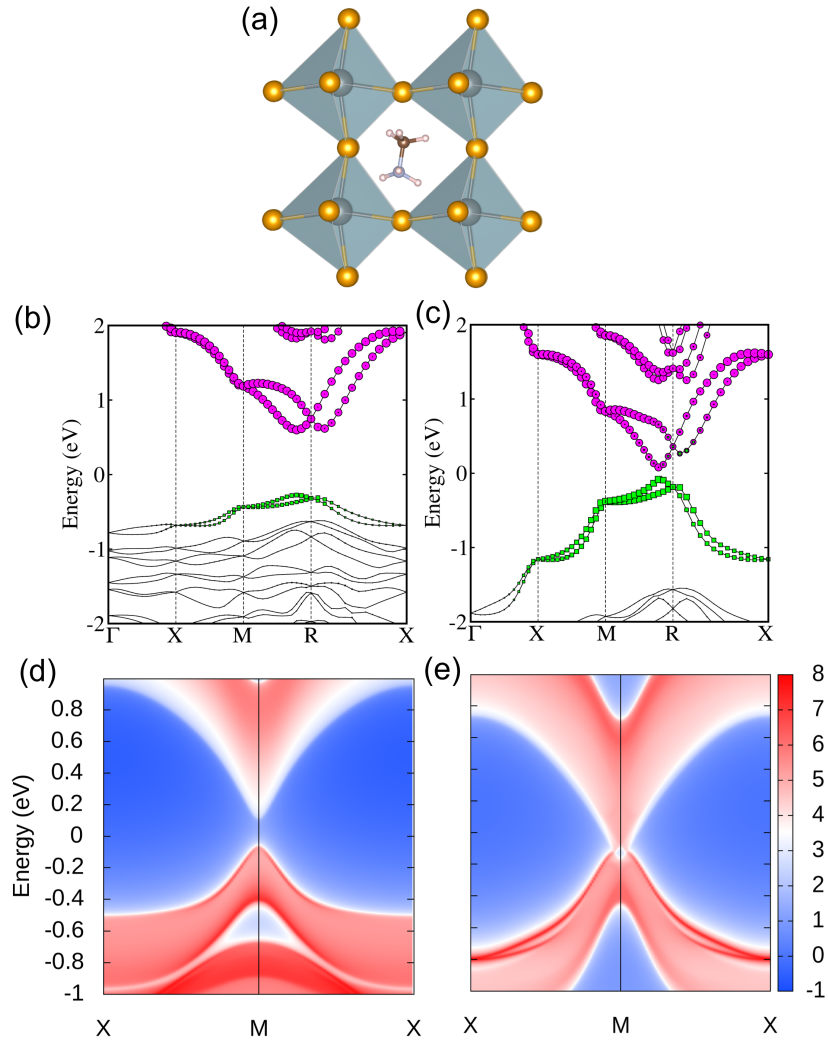


Figure S5: (a) Crystal structure of pseudocubic MAPbI₃. Bulk band structure (b) without compression with Pb-*p* contribution at CBM and Pb-*s* contribution at VBM, and (c) with compression $\gamma=0.73$, showing band inversion at R point. Surface band structure (d) without, and (e) with compression $\gamma=0.73$, showing a discontinuous transition from normal to topological state.

Crystal structures and structural stability of $\text{Cs}_{0.5}\text{MA}_{0.5}\text{PbI}_3$, $\text{Cs}_{0.75}\text{MA}_{0.25}\text{PbI}_3$ and $\text{Cs}_{0.25}\text{MA}_{0.75}\text{PbI}_3$.

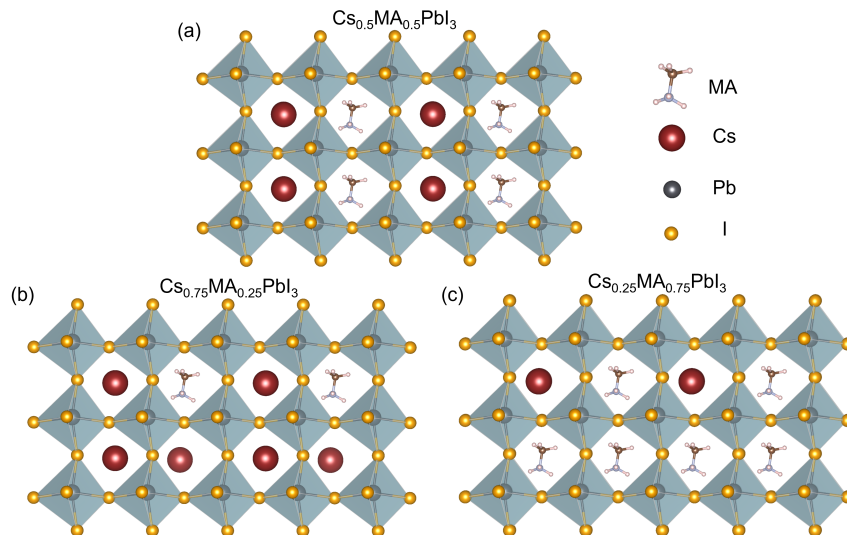


Figure S6: Crystal structure of (a) $\text{Cs}_{0.75}\text{MA}_{0.5}\text{PbI}_3$, (b) $\text{Cs}_{0.5}\text{MA}_{0.5}\text{PbI}_3$ and (c) $\text{Cs}_{0.25}\text{MA}_{0.75}\text{PbI}_3$.

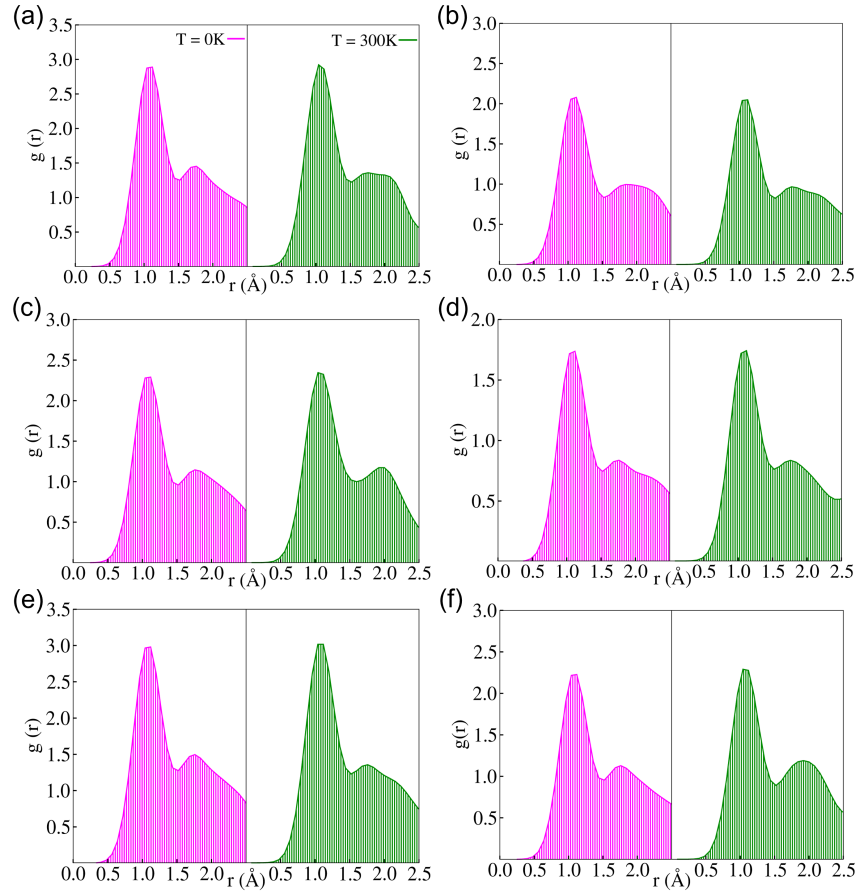


Figure S7: Radial distribution function at $T = 0\text{K}$ and $T = 300\text{K}$ for uncompressed and compressed ($\gamma = 0.74$), (a), (b) $\text{Cs}_{0.5}\text{MA}_{0.5}\text{PbI}_3$, (c), (d) $\text{Cs}_{0.75}\text{MA}_{0.25}\text{PbI}_3$, (e) and (f) $\text{Cs}_{0.25}\text{MA}_{0.75}\text{PbI}_3$, respectively.

TB parameters for $\text{Cs}_{0.5}\text{MA}_{0.5}\text{PbI}_3$.

Table S1: Interaction parameters and SOC strength for $\text{Cs}_{0.5}\text{MA}_{0.5}\text{PbI}_3$ from thirteen band hamiltonian at zero and critical compression strength in units of eV.

Type	E_{Pb-s}	E_{Pb-p}	E_{I-p}	$t_{sp\sigma}^{Pb-I}$	$t_{pp\sigma}^{Pb-I}$	$t_{pp\pi}^{Pb-I}$	$t_{ss\sigma}^{Pb-Pb}$	$t_{sp\sigma}^{Pb-Pb}$	$t_{pp\sigma}^{Pb-Pb}$	$t_{pp\pi}^{Pb-Pb}$	λ
$\gamma = 1$	-7	2	-1.5	0.8	-1	1	-0.25	0.3	0.7	0.01	0.5
$\gamma = 0.74$	-7	2.5	-2	1	-1.2	1.5	-0.27	0.4	1.15	0.02	0.5